ACS Catalysis

pubs.acs.org/acscatalysis

Research Article

Insights into the Nature of Selective Nickel Sites on Ni/Al_2O_3 Catalysts for Propane Dehydrogenation

Rui Ma,*[,∥] Junxian Gao,[∥] Jiajing Kou,[∥] David P. Dean, Christian J. Breckner, Kaijun Liang, Bo Zhou,* Jeffrey T. Miller,* and Guojun Zou

Cite This: *ACS Catal.* 2022, 12, 12607−12616

Read Online

ACCESS | Metrics & More | Article Recommendations | Supporting Information

ABSTRACT: Nickel has been considered a promising nonprecious metal for propane dehydrogenation (PDH) because of its appealing ability to activate alkane molecules; however, synthesis of selective and stable Ni sites remains a challenge. Herein, we describe an alumina-supported isolated Ni(II) site by settling Ni^{2+} cations into Al^{3+} vacancy on γ-Al_2O_3 as a selective and stable Ni-based catalyst for PDH. Based on the results from combined characterizations, including in situ X-ray adsorption spectroscopy (XAS), scanning transmission electron microscopy (STEM), and in situ diffuse reflectance infrared Fourier-transform spectroscopy (DRIFTS), atomically dispersed Ni(II) sites with bonding to oxygen ions from the alumina support are demonstrated. PDH catalyst tests shows that the Ni(II) single-site catalyst delivers superior performance compared to a supported metallic Ni NP catalyst, possessing >93% propylene selectivity at considerable propane conversions (15−45%), which surpasses Ni nanoparticle (NP) catalysts. The correlation of selectivity to propylene on different Ni structures with the structural characterizations suggest that the coordinatively unsaturated tetrahedral Ni(II) sites facilitate the desorption of propylene, which inhibits the side reactions for coking. Moreover, the atomically dispersed Ni(II) sites remain in its local structure in the reaction-regeneration cycles, as evidenced by in situ XAS. This study on alumina-supported nickel catalysts affords insights into the nature of selective and stable nickel sites involved in the PDH reaction.

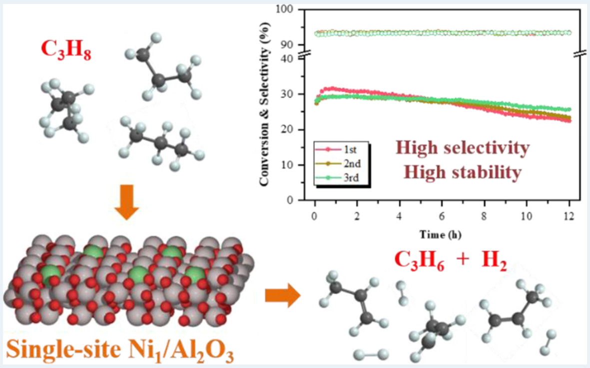

KEYWORDS: *propane dehydrogenation, Ni/Al_2O_3 catalysts, Al^{3+} vacancy, Ni(II) single site, coke deposition*

1. INTRODUCTION

Propylene is an essential platform chemical for the production of polypropylene and other important industrial chemicals and is mainly produced as a byproduct from steam or thermal cracking of naphtha.[1−3] With the increasing production of propane from shale gas, the process of direct dehydrogenation of propane into propylene has attracted attention as a promising route for on-purpose production of propylene. The reaction of PDH ($C_3H_8 \rightleftharpoons C_3H_6 + H_2$) is highly endothermic and thermodynamically limited, so high temperatures are typically required (>550 °C).[4,5] However, at these high reaction temperatures, cracking of C−C bonds, or hydrogenolysis, lowers the propylene selectivity and produces coke.[6] Therefore, practical PDH catalysts must be selective at considerable propane conversions, structurally stable under operation, and recoverable during regeneration cycles. Alumina-supported Pt−Sn and CrO_x catalysts have been used in commercial PDH processes because of their high selectivity of C−H vs C−C bond activation and long performance life.[7−9] However, the high cost of noble Pt and the environmental toxicity of Cr^{6+} species have driven the development of alternative catalysts for PDH.

Generally, the reaction of PDH is thought to be a structure-insensitive reaction which requires only one active atom to catalyze, while deeper dehydrogenation and C−C cleavage involve pathways on the multiatom metallic ensemble sites.[10] Theoretical calculations and experimental tests have demonstrated that decreasing the Pt particle size to atomically dispersed atoms can significantly improve the turnover frequency of alkane dehydrogenation reactions while maintaining superior propylene selectivity and catalytic stability.[11−15] Thus, synthesis of isolated metal sites through alloy formation has emerged as a practical strategy to inhibit undesired side reactions and enhance dehydrogenation performance of catalysts. For instance, promoter addition, such as Sn, Zn, Ce, Ga, Cu, and so forth, leads to higher olefin selectivity and lower coke formation by isolation of Pt atoms in

Received: July 5, 2022
Revised: September 21, 2022
Published: October 3, 2022

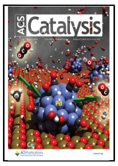

https://doi.org/10.1021/acscatal.2c03240

ordered bimetallic alloy structures and adjusting the energy of the Pt valence orbitals.[16−25] Another approach is the development of supported single-site catalysts, including Co^{2+}, Zn^{2+}, Sn^{2+}, and Ga^{3+}.[26−32] Such metal-O-support sites provide an appropriate barrier for C−H activation and facilitate propylene desorption to inhibit the formation of coke, showing potential for next-generation PDH catalysts.

Alternatively, Ni-based catalysts have garnered interest because of its appealing ability to activate alkane molecules. Nevertheless, supported metallic Ni NP catalysts exhibit a high intrinsic activity toward C−C breaking, leading to the formation of methane, hydrogen, and coke.[33,34] Previous strategies for minimizing the C−C cleavage, such as adding P and S promoters to dilute the large nickel ensembles have been shown to work but suffer from the loss of promoters at high temperatures during the regeneration process.[35−38] By means of anchoring Ni precursors on defect-containing supports, such as heteroatom-doped sp^2 carbon materials, metal organic frameworks (MOFs), and two-dimensional layered MoS_2, supported nickel single-site catalysts for electro-catalysis and other reactions under mild conditions have been reported.[39−41] To date, it remains a challenge to prepare supported nickel catalysts in an exclusively single-site configuration and prevent the reduction of Ni(II) and formation of Ni NPs under the rigorous reaction and regeneration conditions of PDH.

The γ-Al_2O_3 structure is generally considered as a defective spinel structure, where the Mg^{2+} atoms have been removed from the $MgAl_2O_4$ structure, leading to the formation of cation vacancies.[42] Simulation studies of γ-Al_2O_3 have shown that structural models with nonspinel site occupancy are energetically more favorable, suggesting that Al^{3+} vacancy-defects can serve as the anchoring sites for metal atoms.[43−46] For example, the group of Datye reported that the γ-Al_2O_3 supported atomically dispersed Pd^{2+} can be prepared by settling Pd ions into the fourfold hollow of a Al^{3+} vacancy and is stabilized through bonding to surface oxygen atoms on γ-Al_2O_3, even after calcination at 700 °C.[47] Hence, we propose that the strong bonding of nickel to oxygen atoms on the crystalline structure of γ-Al_2O_3 might prevent the reduction and sintering of isolated nickel cations.

Herein, we report that a sintering-resistant Ni(II) single-site catalyst with commercial γ-Al_2O_3 as the support can be achieved via a simple and scalable impregnation method. Atomically dispersed nickel ions, which are stabilized by bonding to oxygen atoms of the Al^{3+} vacancy, are identified by combined characterizations, including X-ray diffraction (XRD), X-ray photoelectron spectroscopy (XPS), scanning transmission electron microscopy (STEM), and in situ X-ray absorption spectroscopy (XAS). We then compare the catalytic performance of the Ni(II) single sites and aggregated metallic Ni toward propane dehydrogenation, revealing that isolated Ni(II) sites are selective and stable for C−H activation, while C−C cleavage involved side reactions are favored on the ensemble of Ni atoms. In situ diffuse reflective infrared Fourier-transform spectroscopy (DRIFTS) of CO adsorption is performed to correlate propylene selectivity with different Ni sites.

2. EXPERIMENTAL METHODS

2.1. Catalyst Preparation. Nickel nitrate hexahydrate (≥99.5%), sodium hydroxide (≥98%), and ammonium hydroxide (25 wt % NH_3) were purchased from Shanghai Aladdin Biochemical Technology Co., Ltd. Boehmite was purchased from Qingdao Haiyang Chemical Co., Ltd. and calcined at 650 °C for 4 h to make Al_2O_3 support. The Al_2O_3 supported Ni NPs catalyst (1 wt %), denoted as Ni_n/Al_2O_3, was prepared using the deposition precipitation method (DP) with NaOH as the precipitator. Typically, 10 g of alumina powder was added to 100 mL of aqueous solution of nickel nitrate (0.51 g) and kept at 60 °C in an oil bath under vigorous stirring. Then, the pH of the mixture was adjusted to 10 by adding the NaOH solution (2 M). After 5 h, the resulting slurry was washed, filtered, and dried at 110 °C overnight, calcined at 600 °C for 4 h, and reduced at 600 °C under 10% H_2/Ar flow for 3 h. To prepare alumina-supported Ni(II) single-site catalyst (Ni_1/Al_2O_3), 0.51 g of nickel nitrate was dissolved in 2.0 mL of deionized water. Then, the pH value of solution was adjusted to 11 by adding ammonium hydroxide, and the volume of impregnated solution was adjusted to 6.5 mL by adding deionized water. The impregnated solution was added dropwise to 10 g of the alumina powder. The resulting sample was dried overnight at 80 °C and then treated at 600 °C under 10% H_2/Ar flow for 3 h. It was noted that the color of the fresh Ni_n/Al_2O_3 and Ni_1/Al_2O_3 catalysts were black and white, respectively, as shown in Figure S1. A $NiAl_2O_4$ phase, as a reference for characterization and reaction evaluation, was prepared by following the procedures reported in our previous work, and TEM characterization of as-prepared $NiAl_2O_4$ NPs is displayed in Figure S2.[48]

2.2. Characterization. The nickel loading of alumina-supported nickel catalysts prepared using different methods was determined by a PerkinElmer ICP 2100. The Brunauer−Emmett−Teller (BET) surface area of samples were measured by N_2 adsorption−desorption experiments performed on Micromeritics ASAP2020 at 77 K. ^{27}Al NMR spectrum of alumina was recorded on a Bruker 400 M spectrometer using a 4-mm MAS BB/1H probe, operating at 104.3 MHz. XRD spectra of samples were obtained using Bruker D8 instrument using Cu K_α as a radiation source by applying a scanning rate of 2°/min in the range of 10−80°. Temperature programmed hydrogen reduction (H_2-TPR) profiles of the Ni-based catalyst precursors were carried out on a AutoChemII 2920 (Micrometrics) using a thermal conductivity detector. About 100 mg of the calcined samples were loaded in a U-shaped quartz reactor and pretreated in N_2 flow at 300 °C for 1 h. The reduction procedure was carried out under 30 mL 10% H_2/Ar flow with a heating rate of 10 °C/min to 1100 °C. The XPS experiment was conducted on a K-Alpha spectrometer (Thermo Scientific) equipped with Al K_α anode. The binding energy of the elements was calibrated by setting the C 1s peak to a binding energy (B.E.) of 284.6 eV. The size of nickel particles and elemental distribution of Ni were analyzed using JEOL-2100F TEM at an acceleration voltage of 200 keV. The high-angle angular dark-field scanning transmission electron microscopy (HAADF-STEM) images of Ni atoms were obtained using Titan Cubed Themis G2300. Thermogravimetric characterization of spent catalysts was carried out on a Bruker TG-DSC instrument under 10% O_2 (50 mL/min) flow, and the temperature ramp rate was 10 °C/min.

The X-ray absorption spectroscopy (XAS) experiments of alumina-supported nickel samples were carried out at the 10-BM-B beamline at the Advanced Photo Source (APS) at Argonne National Laboratory. The Ni K-edge XAS spectra were collected in transmission mode using three ion chambers which allowed simultaneous measurement of the samples and a

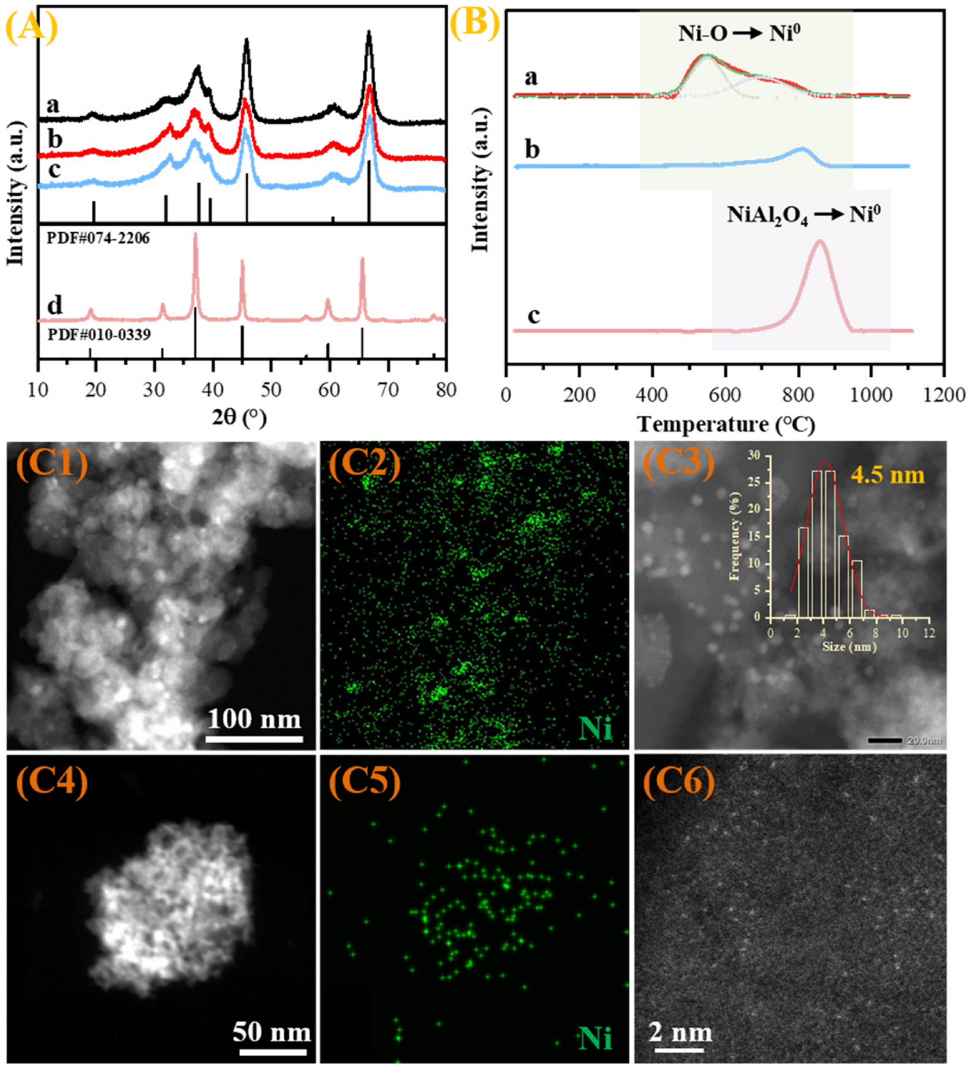

Figure 1. (A) XRD patterns of the (a) Al_2O_3, (b) Ni_n/Al_2O_3 catalyst, (c) Ni_1/Al_2O_3 catalyst, and (d) $NiAl_2O_4$ NPs. (B) H_2-TPR profiles of (a) Ni_n/Al_2O_3, (b) Ni_1/Al_2O_3, and $NiAl_2O_4$ NPs precursors after calcination in air. (C) TEM images of Ni_n/Al_2O_3 (C1−C3) and Ni_1/Al_2O_3 catalyst (C4−C6).

Ni foil reference. Each sample was ground into powder and pressed into a self-supporting wafer inside of a stainless-steel sample holder, which was loaded into a quartz tube reactor. The reactor was heated at 600 °C in 3% H_2/Ar flow for 1 h. Then, the reactor was purged with He flow, and the scans were collected at room temperature. Scans were also collected for the Ni_1/Al_2O_3 catalyst after treatments in 3% C_3H_8/He at 580 °C for 1 h and 20% O_2/He at 600 °C for 1 h. XAS data were processed with Demeter package and WinXAS software.[49] Simulated phase and amplitude functions for Ni−O, Ni−Al, and Ni−Ni scattering were extracted using FEFF. The extracted chi was k^2-weighted and Fourier-transformed over a k range of 2.5−10.0 $Å^{-1}$ for oxides. The S_0^2 term was determined by fitting the spectrum of experimental NiO reference compound, and the value was fixed for all samples. Fitting was performed in q space to determine the Debye−Waller factor σ^2, and then performed in R space (allowing the coordination number, bond distance, and E_0 correction to vary) to determine the coordination number and bond distance.

In situ diffuse reflectance infrared Fourier-transform spectra (In situ DRIFTS) were collected on a Tensor II (Bruker) spectrometer equipped with an MCT detector. A ZnSe window sealed diffuse reflectance chamber was taken to treat sample in controlled atmospheres and temperatures, which was connected to a vacuum system to control pressure. Prior to CO adsorption, pressed disks of fresh catalysts were pretreated at 600 °C for 1 h under 30 mL/min H_2/Ar flow (10%) and cooled to a low temperature (~125 K) under a dynamic vacuum (10^{-5} mbar). IR spectra of background and CO adsorption were acquired in the 800−3200 cm^{-1} range by collecting 128 scans at a resolution of 4 cm^{-1}. Commercial software (Bruker OPUS 8.5) was used to analyze data, and the spectra were converted to Kubelka−Munk spectra after baseline and offset corrections.

2.3. Catalytic Evaluation. Propane dehydrogenation was performed in a fixed-bed quartz micro-reactor (6 mm inner diameter) with 0.5 g of sample (40−60 mesh) loaded. The catalysts were pretreated in diluted hydrogen gas flow at 600 °C for 1 h and then cooled to test temperature under N_2 flow. The input gas contains 20% propane, balanced with nitrogen. The gas flow rate was 20 mL/min, controlled using a mass flowmeter (Bruker), to give a weight hourly space velocity of propane (WHSV) of 0.3 h^{-1}. The composition of outgas was

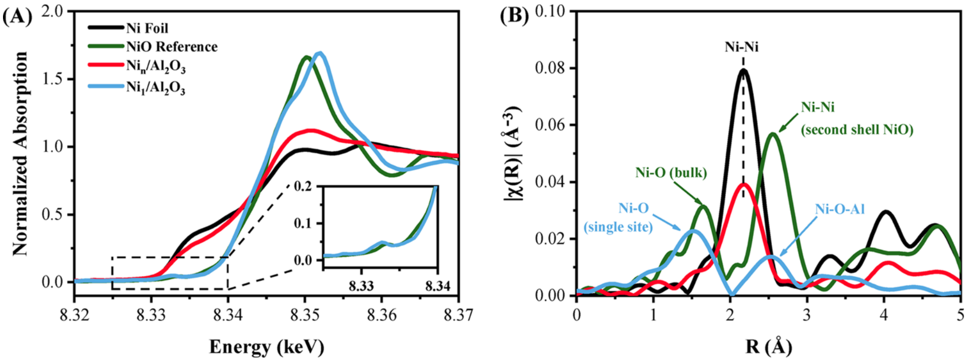

Figure 2. Ni K-edge (A) XANES spectra, including inset for zoomed-in pre-edge feature, and (B) FT magnitude of the k^2-weighted EXAFS in R space for Ni_n/Al_2O_3 and Ni_1/Al_2O_3 catalysts, with comparison to a Ni foil and a NiO reference.

determined by online gas chromatography (Agilent 8890) equipped with an FID detector. The conversion of propane and selectivity of propylene were determined by the equations below. As a comparison, the thermodynamic equilibrium of propane conversion at each temperature was calculated by the commercial software Aspen Plus. Based on the mass balance between carbons in the introduced and the produced hydrocarbons, the carbon balance of alumina-supported nickel catalysts during dehydrogenation was calculated, as shown in Figure S3. The amount of coke deposition on spent catalysts was determined by thermogravimetric characterization. The regeneration of spent catalysts was repeated twice. Dried air was switched into the reactor after each PDH run. Herein, the turnover frequency (TOF) of catalysts is defined as the moles of converted propane per mole of active atoms per second, assuming that Ni dispersion of Ni_1/Al_2O_3 is 100%. The metal dispersion (D) of Ni_n/Al_2O_3 is determined basing on the average size (d) of Ni NPs, using the formula described in the previous work, and gives a 24.9% Ni dispersion over the Ni_n/Al_2O_3 catalyst.[50] The apparent activation energy (E_a) was determined by Arrhenius plots under low propane conversions (4−10%) by adjusting the test temperature.

$$\text{Conv (\%)} = \frac{\text{moles of propane ininlet} - \text{moles of propane in outlet}}{\text{moles of propane in inlet}} \times 100\%$$

$$\text{Sel (\%)} = \frac{\text{moles of propylene}}{\text{moles of propylene} + \frac{2\times\text{moles of C2}}{3} + \frac{\text{moles of methane}}{3}} \times 100\%$$

A first-order model was used to calculate the deactivation rate (k_d) within 12 h reaction, as shown in the following equation, Conv_0 and Conv_t are the initial and final conversions, respectively.[51]

$$k_d = \frac{\ln\left(\frac{100 - \text{Conv}_t}{\text{Conv}_t}\right) - \ln\left(\frac{100 - \text{Conv}_0}{\text{Conv}_0}\right)}{t}$$

3. RESULTS AND DISCUSSION

3.1. Preparation and Characterization of Alumina-Supported Ni(II) Single-Site Catalyst.

Alumina, a widely used material for industrial catalysts, which is functional, thermostable, and environmentally friendly, is also the preferred choice for PDH commercial catalysts. In this work, γ-Al_2O_3 supported nickel catalysts, Ni_n/Al_2O_3 and Ni_1/Al_2O_3, were prepared using DP and incipient wetness impregnation (IWI) methods, respectively. During impregnation, the pH of Ni-containing impregnation solution was adjusted to 11 by NH_4OH, which leads to the deprotonation of the surface of γ-Al_2O_3, allowing the $Ni(NH_3)_6^{2+}$ species to be electrostatically adsorbed on the O^{n-} sites located at the Al^{3+} vacancies. The similar loadings (∼1 wt %) for both samples are determined by inductively coupled plasma-atomic emission spectroscopy (ICP-AES). The XRD patterns of the alumina support and alumina-supported nickel catalysts prepared from different methods are illustrated in Figure 1A. The typical diffraction peaks at $2\theta = 19.6°$, 31.9°, 37.6°, 39.5°, 45.8°, 60.5°, and 66.8° of the alumina support can be assigned to the crystal phase of γ-Al_2O_3 (PDF#074-2206).[52] The size of alumina particles is calculated to be 13.4 nm using the Scherrer equation, which matches the statistical size measured from TEM images, as shown in Figure S4. Comparing the spectrum of alumina support with those of Ni-based catalysts, we can find that the loading of nickel does not change the overall structure of the alumina. It should be noted that a slight shift to a lower angle of diffraction peaks on Ni_1/Al_2O_3 is observed. Specifically, Figure S5 shows the magnified XRD pattern of three samples in the 41−50° region and the change of the lattice parameters of alumina as a function of Ni addition. For the Ni_1/Al_2O_3 sample, the shift of the <400> reflection of alumina to a lower 2θ value corresponds to the increase in the lattice parameter (a) from 7.87 to 7.90 Å, suggesting the successful incorporation of Ni in the γ-Al_2O_3 structure, while the Ni_n/Al_2O_3 sample shows no change in the corresponding peak position. The absence of diffraction signals of Ni species on both catalysts suggests high dispersion of nickel on the γ-Al_2O_3 support. As a reference, $NiAl_2O_4$ (PDF#010-0339) is the only detected phase matching the diffraction peaks of $NiAl_2O_4$ NPs, as displayed in Figure 1A(f).[53] More physicochemical properties of alumina and Ni-based catalysts, including BET and ^{27}Al NMR analysis are described in Figure S6 and Table S1.

The H_2-TPR characterization is carried out to study the reducibility of Ni species on alumina-supported nickel samples, and the results are displayed in Figure 1B. In terms of the Ni_n/Al_2O_3 precursor, a broad overlapped H_2-consumption peak can be assigned to the reduction of NiO to metal Ni. According to the previous studies on alumina-supported nickel catalysts, it can be roughly defined that the two reduction peaks (551 and 700 °C) refer to the nickel oxide with medium and strong interaction to alumina, respectively.[54,55] In addition, metallic Ni species are detected by XPS characterization on the fresh Ni_n/Al_2O_3 catalyst, as shown in Figure S7. The alumina-supported Ni sample prepared from the IWI method exhibits only one reduction peak at 810 °C, which is close to the reduction of cationic nickel from the $NiAl_2O_4$ crystal phase (851 °C). Moreover, the reduction peak area of oxidation nickel species on Ni_1/Al_2O_3 precursor is much smaller than that of Ni_n/Al_2O_3, suggesting that the nickel bonding to oxygen atoms maintains its structure even after reduction at 1100 °C. Consistently, the XPS spectrum of the Ni_1/Al_2O_3 catalyst (Figure S7) only shows a single Ni $2p_{3/2}$ peak locating at 856.1 eV, which is attributed to the Ni^{2+} species.[56]

The atomic-scale structure of the Ni species was further characterized by STEM analysis (Figure 1C). For the Ni_n/Al_2O_3 catalyst, the formation of Ni NPs with a clear crystalline structure is observed, and the average size of the Ni NPs is 4.5 nm (Figure 1C1−C3). On the contrary, no obvious Ni aggregation on the Ni_1/Al_2O_3 catalyst was detected in both the STEM image and the corresponding energy-dispersive X-ray spectroscopy (EDX) maps (C4 and C5). By increasing the magnification, exclusively isolated Ni atoms uniformly dispersed on the alumina surface as bright dots are observed in HAADF-STEM image, as shown in Figure 1C6.

XAS characterization was employed to reveal the chemical environment of different nickel species. Figure 2 shows the X-ray absorption near edge structure (XANES) and the X-ray absorption fine structure (EXAFS) spectra for the two alumina-supported nickel catalysts as well as Ni foil (Ni^0) and NiO (Ni^{2+}) references. The model fits for all of the samples and references are displayed in Figure S8. The XANES spectrum of Ni_n/Al_2O_3 shows a similar edge energy (8332.6 eV) to a Ni foil (Table 1), but the white line intensity is higher due to a small proportion of the Ni remaining oxidized. The EXAFS of Ni_n/Al_2O_3 displays one main peak at the same bond distance as Ni−Ni in the Ni foil, but with a smaller FT magnitude due to lower coordination, as well as a smaller shoulder at lower R (Figure 2B). Upon fitting, Ni−Ni coordination is found to be 8.3, and Ni−O coordination is found to be 1.3 at the Ni−O single site bond distance of 2.01 Å, suggesting the presence of a small proportion of Ni^{2+} that does not reduce after treatment at 600 °C in H_2. The XANES of the Ni_1/Al_2O_3 sample is similar to that of the NiO (Ni^{2+}) reference, including the pre-edge feature near 8333 eV, as highlighted in the inset of Figure 2A. The pre-edge peak is assigned to the dipole-forbidden but quadrupole-allowed transition ($1s \rightarrow 3d$).[57] The pre-edge feature has been previously reported to shift to lower energy going from octahedral to tetrahedral Ni, owing to the fact that the half-filled orbitals in an octahedral geometry have a higher energy than the half-filled t_2 orbitals in a tetrahedral geometry.[58] It can be seen from Figure 2A and Table 1 that the edge energy of Ni_1/Al_2O_3 is centered at a higher energy than that of NiO reference, suggesting that the energy required for an electron transition from $1s$ to $4p$ is higher for Ni species supported on γ-Al_2O_3.[59] This may be due to the strong interaction between the support and Ni species. The EXAFS for NiO exhibits prominent peaks at around 2 and 3 Å, which correspond with first-shell Ni−O coordination and second shell Ni−Ni coordination (Figure 2B). EXAFS fitting for NiO, as shown in Table 1, yields a first-shell Ni−O coordination of 6.0 at a bond distance of 2.09 Å and a second shell Ni−O−Ni coordination of 12. Also, as shown in Figure 2B, the EXAFS for Ni_1/Al_2O_3 appears to have a smaller FT magnitude (lower coordination) at a shorter bond distance compared to the NiO reference. This is confirmed by the first-shell fitting results, which assert a Ni−O coordination of 4.3 at a bond distance of 2.01 Å (Table 1). For the second shell EXAFS, it can be difficult to discern the difference between Ni−O−Ni and Ni−O−Al scattering based on the real portion of the FT magnitude EXAFS spectrum because of the small magnitude of the peak. Nevertheless, the imaginary portion of the FT magnitude EXAFS is qualitatively different between the Ni_1/Al_2O_3 sample and the NiO reference (Figure S9), suggesting the presence of a different scattering path. The second shell fitting results in Figure S9 and Table S2 illustrate that the second shell scattering can be attributed to Ni−O−Al scattering as opposed to Ni−O−Ni scattering. Holding the first-shell fitting parameters constant, the second shell parameters of coordination number, bond distance, and ΔE_o were allowed to vary. The fit using Ni−O−Al and the fit using Ni−O−Ni both have a low least squares error for the second shell, but the Ni−O−Ni fit results in an unrealistic ΔE_o value of −15.7 eV compared to the Ni−O−Al fit that yields a more realistic ΔE_o value of 3.6 eV. All other things being equal, the second shell scattering can be assigned to Ni−O−Al scattering with a coordination of 4.0 at a bond distance of 2.88 Å. Based on the collective evidence, the Ni in Ni_1/Al_2O_3 is present as isolated Ni(II) single sites, which are anchored on the surface of γ-Al_2O_3 through bonding to oxygen atoms, while the Ni atoms in Ni_n/Al_2O_3 are mostly incorporated into metallic Ni NPs.

Table 1. Ni K-Edge XAS Fitting Parameters for Alumina-Supported Nickel Catalysts

sample	edge energy (eV)	scatter	CN	R (Å)	ΔE_0 (eV)	σ^2
Ni foil	8333.0	Ni−Ni	12.0	2.48	5.1	0.005
NiO ref.	8340.6	Ni−O	6.0	2.09	2.4	0.005
		Ni−O−Ni	12.0	2.94	−3.0	0.005
Ni_n/Al_2O_3	8332.6	Ni−O	1.3	2.01	6.6	0.005
		Ni−Ni	8.3	2.47	4.3	0.007
Ni_1/Al_2O_3	8342.0	Ni−O	4.3	2.02	1.0	0.005
		Ni−O−Al	4.1	2.88	3.6	0.007
2.5%-Ni_1/Al_2O_3	8342.1	Ni−O	4.3	2.02	1.4	0.005
		Ni−O−Al	4.0	2.88	3.9	0.007
Ni_1/Al_2O_3 (C_3H_8)	8342.1	Ni−O	4.4	2.00	−3.7	0.005
Ni_1/Al_2O_3 (O_2)	8342.1	Ni−O	4.4	2.01	−3.3	0.005

The surface properties of γ-Al_2O_3 are strongly influenced by its bulk structure and surface hydroxyl groups. Thus, IR spectroscopic experiments of CO adsorption were performed to study the interaction between γ-Al_2O_3 and nickel species, and hence the resulting active centers. The samples were pretreated at 600 °C in hydrogen flow to activate the samples, and the IR spectra of CO adsorption at low temperature under increasing pressure on γ-Al_2O_3 and supported nickel catalysts are compared in Figure 3. The vibrational features of adsorbed-CO at 2157 cm^{-1} with a shoulder at 2135 cm^{-1} over γ-Al_2O_3

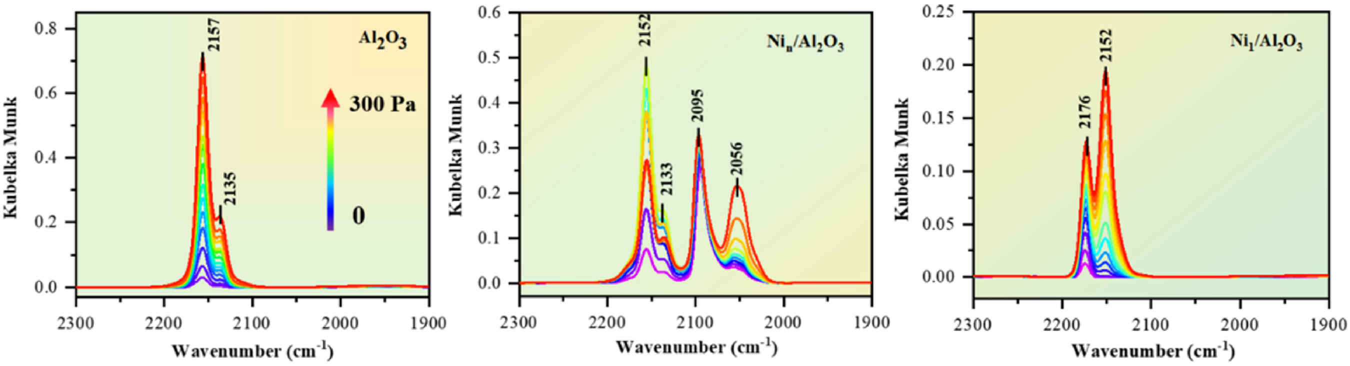

Figure 3. Infrared spectra of CO adsorbed at low temperature (125 K) on γ-Al_2O_3 and Ni-based catalysts. Before CO adsorption, all samples were outgassed to below 10 Pa under high vacuum, then the spectra of CO adsorption were recorded under increasing pressure from 30 to 300 Pa.

are observed, attributing to CO interaction with OH groups and weak physisorption at low temperature, respectively, and the intensity of both peaks increases with increasing CO pressure.[60] Introduction of low pressure CO (40 Pa) to the Ni_n/Al_2O_3 catalyst results in the appearance of two new intense bands at 2095 and 2056 cm^{-1}, which are attributed to the terminally bonded CO on low-coordinated and saturation-coordinated Ni^0 atoms, respectively.[61−63] As the CO pressure increased, the intensity of the peak at 2056 cm^{-1} gradually increased, while the intensity of the peak at 2095 cm^{-1} remains largely unchanged. The change of peak intensity with CO pressure implies that CO preferentially adsorbs to low-coordinated Ni^0 atoms because of the higher adsorption enthalpy, including atoms located at corners, edges, and terraces on Ni NPs, which may possess higher activity for the activation of propane molecules.[64] In the case of the Ni_1/Al_2O_3 catalyst, no relative features of metallic Ni bonded CO are detected, and an intense peak emerges at 2175 cm^{-1}. The ν_{CO} is expected to shift to a higher wavenumber with increasing polarizing power of the cation, so the adsorbed-CO at 2175 cm^{-1} belongs to the stretching vibration of CO on Ni^{2+} sites.[65] In addition, the disappearance of physisorbed CO and the decrease of hydroxyl groups interacting with CO are notable for the Ni_1/Al_2O_3 catalyst, suggesting a change in the surface properties of γ-Al_2O_3. Likely, impregnation of the deprotonated γ-Al_2O_3 with $Ni(NH_3)_6^{2+}$ affects the hydroxyl groups, functioning as surface germination sites during the impregnation step. The following thermal and reduction treatments do not restore the initial hydroxyl groups on the support, and this effect serves as evidence of a significant nickel−alumina interaction.[66,67]

In summary, all characterizations discussed above demonstrate that the atomically dispersed Ni^{2+} cations are successfully incorporated into the crystalline structure of γ-Al_2O_3 using a facile impregnation method. In addition, a higher nickel loading of the Ni_1/Al_2O_3 can be achieved while maintaining a Ni(II) single site structure. A supported Ni(II) single-site catalyst containing 2.5% nickel was prepared using the same procedures, and the sample is denoted as 2.5%-Ni_1/Al_2O_3. The EXAFS of the 2.5%-Ni_1/Al_2O_3 is identical with Ni_1/Al_2O_3 (Figures 4, S13 and Table 1). The EXAFS fitting for the 2.5%-Ni_1/Al_2O_3 sample, after treatment in 3% H_2 at 600 °C, fits well using Ni−O and Ni−O−Al scattering paths, resulting in a Ni−O coordination number of 4.3 at a bond distance of 2.02 Å, indicating fully isolated Ni^{2+} cations at the higher weight loading. Given the generality of alumina-supported nickel catalysts for heterogenous catalysis, this facile and scalable method to obtain atomically dispersed Ni species offers opportunities to enhance the catalytic performance of other reactions.

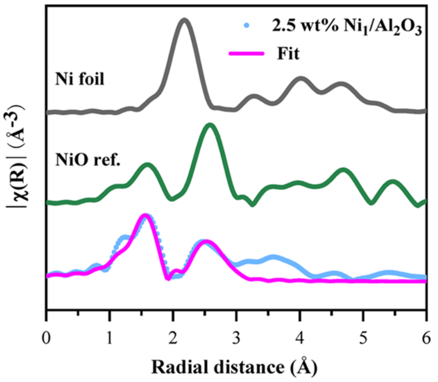

Figure 4. Ni K-edge k^2-weighted magnitude of the EXAFS in R space for Ni_1/Al_2O_3 catalysts with 2.5 wt % Ni loading.

3.2. Catalytic Performance of Propane Dehydrogenation.

We then evaluate the direct dehydrogenation of propane for Ni_1/Al_2O_3, Ni_n/Al_2O_3, and $NiAl_2O_4$ NPs to compare the catalytic properties of different nickel species. The catalytic activity of blank alumina is also tested in the range of 550−600 °C, as shown in Figure S10, where the initial conversions of propane are below 3% and the selectivity to propylene decreases with increasing temperature from 550 to 600 °C (61 to 48%). In Figure S11, the Ni_n/Al_2O_3 catalyst shows a high initial propane conversion (89%), giving a TOF of 0.076 s^{-1} at 580 °C. In terms of the product distribution, methane is the main product at the beginning of the test and only 4.8% selectivity toward propylene is detected. The primary product rapidly shifts toward propylene as the reaction proceeds, and 65% selectivity to propylene at 5.9% propane conversion is obtained after 12 h. The activity of the Ni_n/Al_2O_3 catalyst, however, sharply decreases to nearly 0.01 s^{-1} after 0.5 h reaction and then slowly decreases with increasing time on stream. The dehydrogenation results for the Ni_1/Al_2O_3 sample exhibits entirely different catalyst performance. Figure 5 shows the propane conversion and selectivity to propylene as a function of time on stream at varied reaction temperatures. The propane conversion significantly increases with increasing the reaction temperature from 550 to 600 °C, from 17 to 43%, without an obvious decline of conversion within 3 h. Simultaneously, the Ni_1/Al_2O_3 shows a resilient high propylene selectivity during each test (>93%) at an appreciable

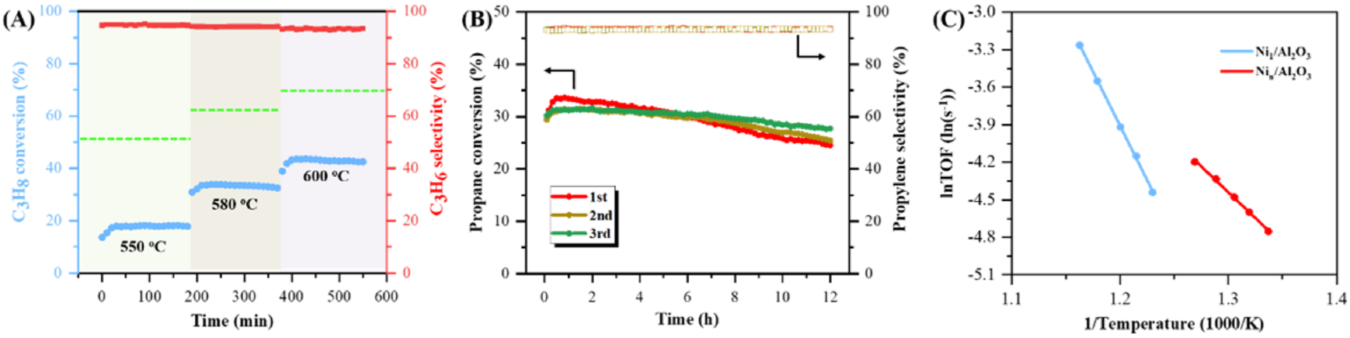

Figure 5. (A) Propane conversion and propylene selectivity over the Ni_1/Al_2O_3 catalyst at different evaluated temperatures, with equilibrium propane conversions marked as the green dotted line. Test conditions: atmospheric pressure, 20 mL/min diluted propane (C_3H_8:N_2 = 1:4) to give a 0.3 h^{-1} WHSV of propane. (B) Ni_1/Al_2O_3 catalyst in the PDH at 580 °C. After each PDH run, the catalyst was regenerated by oxidative treatment using dried air (40 mL/min) for 1 h at 600 °C, and then purged by pure nitrogen gas cooled to 580 °C. (C) Arrhenius plots for propane conversion over alumina-supported nickel catalysts, 4−10% propane conversions were recorded by adjusting the test temperature and sample loadings in the reactor.

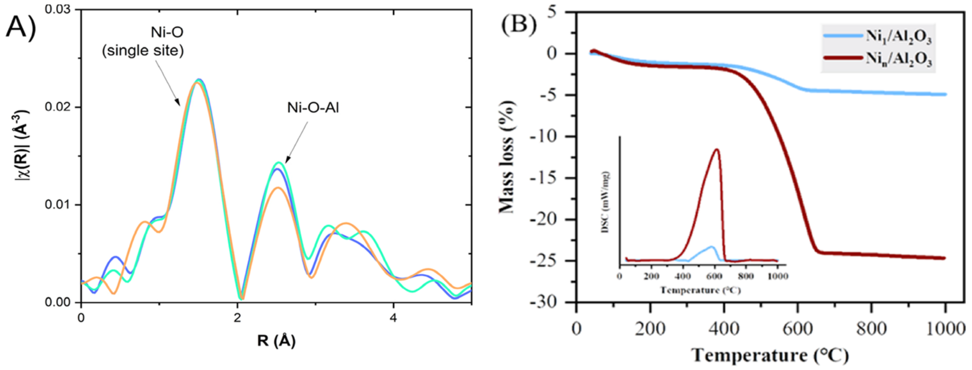

Figure 6. (A) k^2-weighted magnitude of the EXAFS in R space for Ni_1/Al_2O_3 catalysts: (a) treated in diluted hydrogen at 600 °C for 1 h, (b) reaction in diluted propane at 580 °C for 1 h, and (c) regeneration in air at 600 °C for 1 h. (B) TG and DSC (inserted) curves of alumina-supported nickel catalysts after 12 h reaction.

propane conversion (>17%). Less than 5% methane was obtained at the highest temperature and conversion (600 °C, 43%). Catalytic dehydrogenation of the Ni_1/Al_2O_3 catalyst under the rigorous conditions of pure propane as well as pure propane co-fed with hydrogen in a 2:1 ratio at 580 °C was also performed, as shown in Figure S12. More importantly, the Ni_1/Al_2O_3 catalyst exhibits good catalytic stability over the course of three reaction-regeneration cycles. As shown in Figure 5B, a high selectivity to propylene (∼93%) is obtained across all reaction runs. In the first run, the propane conversion decreased from 29.4 to 24.5% during 12 h, and the deactivation rate (k_d) is calculated to be 0.021 h^{-1}. It is worth mentioning that the rate of propane conversion decline decreases after each regeneration, and the deactivation rates of 0.017 and 0.012 h^{-1} are obtained during second and third runs, respectively. In contrast, Ni_n/Al_2O_3 deactivates quickly, giving a high k_d value of 0.427 h^{-1}. These results indicate that the catalytic performance of the Ni_1/Al_2O_3 catalyst can be completely recovered after the regeneration of the catalyst, and this remarkable stability of the Ni_1/Al_2O_3 catalyst for propane dehydrogenation is comparable to the reported Pt-based alloy catalysts.[11,17,21,23]

We then compare apparent activation energies of Ni_1/Al_2O_3 and Ni_n/Al_2O_3 catalysts by plotting ln(TOF) versus $1/T$, as shown in Figure 5C. The E_a value for PDH over the Ni NPs catalyst is 71.2 kJ/mol, which is lower than those of the reported Pt and Pt-based alloy catalysts.[11,16,68] A higher E_a value for Ni_1/Al_2O_3 catalyst is observed (143.8 kJ/mol), which is comparable to reported metal oxide PDH catalysts (130−180 kJ/mol).[26,59,69] The significant increase of E_a for the single site catalyst, compared to the Ni NPs catalyst, explains the initial PDH performance for these two catalysts.

The ability to resist reduction and aggregation is quite important for structural stability of the Ni(II) single-site catalyst. In situ XAS experiments of the Ni_1/Al_2O_3 catalyst during the reaction-regeneration process were conducted to reveal the specific changes of the Ni_1/Al_2O_3 catalyst. The Ni_1/Al_2O_3 catalyst after 1 h treatment in 3% H_2 at 600 °C, 1 h treatment in 3% C_3H_8 at 580 °C, and 1 h treatment in 20% O_2 at 600 °C is qualitatively identical irrespective of gas treatment as illustrated by the R space and k-space EXAFS spectra (Figures 6A and S14). The first-shell EXAFS fitting results are given in Table 1, showing a Ni−O coordination number of either 4.3 or 4.4 at a bond distance of 2.00 or 2.01 Å for all of the treatments. Regardless of gas treatment, the nature of the Ni sites remains constant for the Ni_1/Al_2O_3 sample. This suggests that the atomically dispersed Ni^{2+} sites retain their local structure and no reduction or aggregation occurs over reaction-regeneration cycles, explaining the high stability of the Ni_1/Al_2O_3 catalyst for PDH. While coordinatively unsaturated (tetrahedral) and isolated Ni(II) site exhibits high performance for PDH, octahedral and isolated Ni^{2+} in unreduced $NiAl_2O_4$ NPs was also tested for PDH (Figure S15) and resulted in a poor PDH activity and propylene selectivity. This suggests that the unsaturation of Ni(II) single site is critical for PDH performance.

In addition to the structural stability, the Ni(II) sites exhibit a surprising ability to resist coke deposition. The amount of coke deposited on both alumina-supported Ni catalysts after PDH run within 12 h was measured using thermogravimetric analysis, and the TG-DSC results are presented in Figure 6B. The amount of coke on the Ni_1/Al_2O_3 and Ni_n/Al_2O_3 catalysts is 2.9% and 22.5% w/w, respectively, corresponding to the mass loss in the temperature range of 300−700 °C. Significantly more coke is produced on metallic Ni NPs because of higher C−C bond breaking rates. As a result, C2 and C1 fragments, along with strongly adsorbed propylene, lead to the formation of aliphatics or graphite compounds in the coke through polymerization reactions.[70,71] Meanwhile, the severe aggregation of Ni NPs also contributes to the rapid deactivation of the Ni_n/Al_2O_3 catalyst. TEM characterization of the spent Ni_n/Al_2O_3 catalyst was performed to study the change of Ni dispersion, and the average diameter of Ni NPs is 8.7 nm (Figure S16), which is almost twice that of the fresh catalyst.

The product distribution analyses suggest that both metallic and oxidized nickel species catalyze the activation of propane molecules, but through different reaction pathways. On supported Ni NPs catalyst, propane molecules adsorb prior to low-coordinated Ni atoms because of the higher enthalpy of adsorption, as illustrated by IR results. However, the strong adsorption of generated propylene and other deeply dehydrogenated species on such sites results in coke deposition, which in turn deactivates the Ni_n/Al_2O_3 catalyst quickly. Thus, the activation of propane mainly occurs on saturated Ni atoms with lower catalytic activity, but weakened desorption of propylene leads to higher propylene selectivity and catalyst stability. The higher propylene selectivity of the Ni_1/Al_2O_3 catalyst is ascribed to the facile desorption of propylene on Ni(II) single sites, which prevents the further conversion of propylene into propylidyne. According to the recent experimental results and DFT calculations, the propylidyne species is a likely intermediate for further decomposition of propylene, which requires a threefold Ni−Ni−Ni site.[33] The active sites identified from CO-IR analysis reasonably explains the evolution of PDH performance on Ni(II) single sites and Ni−Ni ensemble sites.

4. CONCLUSIONS

In summary, we report that atomically dispersed Ni(II) with varied nickel loadings can be prepared by anchoring Ni atoms into Al^{3+} vacancies on γ-Al_2O_3, which serves as a selective and stable catalyst for propane dehydrogenation. Structural elucidation of Ni sites on alumina, by in situ XAS, HAADF-STEM, and CO-IR analysis indicates that the tetrahedral Ni(II) single sites account for the significantly higher propylene selectivity and catalytic stability compared to a Ni NPs catalyst. The Ni(II) single-site catalyst exhibits >93% propylene selectivity with a 0.012 h^{-1} deactivation rate in PDH reaction at 580 °C. More importantly, its structural stability and significantly reduced coking rate ensure the complete recovery of catalytic performance after regeneration of the spent catalyst. This study on Ni-based catalysts provides insights into the nature of robust Ni sites for propane dehydrogenation and demonstrates that unsaturated Ni(II) single site catalysts can serve as a promising substitute of noble Pt catalysts for PDH.

■ ASSOCIATED CONTENT

Supporting Information

The Supporting Information is available free of charge at https://pubs.acs.org/doi/10.1021/acscatal.2c03240.

Characterizations of alumina support, Ni catalysts, and catalytic results; characterizations include TEM, XRD, EXAFS, BET, and propane dehydrogenation reactions of the catalysts (PDF)

■ AUTHOR INFORMATION

Corresponding Authors

Rui Ma − *Chemistry and Chemical Engineering Guangdong Laboratory, Shantou 515031, China;* orcid.org/0000-0002-4841-0047; Email: marui1840@163.com

Bo Zhou − *Chemistry and Chemical Engineering Guangdong Laboratory, Shantou 515031, China;* orcid.org/0000-0003-2660-1384; Email: zhoubo8804@126.com

Jeffrey T. Miller − *Davidson School of Chemical Engineering, Purdue University, West Lafayette, Indiana 47907, United States;* orcid.org/0000-0002-6269-0620; Email: mill1194@purdue.edu

Authors

Junxian Gao − *Davidson School of Chemical Engineering, Purdue University, West Lafayette, Indiana 47907, United States;* orcid.org/0000-0002-1015-7103

Jiajing Kou − *College of Vehicles and Energy, Yanshan University, Qinhuangdao 066000, China*

David P. Dean − *Davidson School of Chemical Engineering, Purdue University, West Lafayette, Indiana 47907, United States*

Christian J. Breckner − *Davidson School of Chemical Engineering, Purdue University, West Lafayette, Indiana 47907, United States;* orcid.org/0000-0002-6573-7762

Kaijun Liang − *Chemistry and Chemical Engineering Guangdong Laboratory, Shantou 515031, China*

Guojun Zou − *Chemistry and Chemical Engineering Guangdong Laboratory, Shantou 515031, China*

Complete contact information is available at: https://pubs.acs.org/10.1021/acscatal.2c03240

Author Contributions

[‖]R.M., J.G. and J.K. contributed equally.

Notes

The authors declare no competing financial interest.

■ ACKNOWLEDGMENTS

This work was supported by the National Natural Science Foundations of China (22102060). Financial support from the Chemistry and Chemical Engineering Guangdong Laboratory for conducting the research is gratefully acknowledged (2111001, 2011001, and 1911023). J.G. and J.T.M. were supported by National Science Foundation under award no. 1804712. D.P.D., C.J.B., and J.T.M. were supported in part by the National Science Foundation under Cooperative Agreement No. EEC-1647722. Use of the Advanced Photon Source was supported by the U.S. Department of Energy Office of Basic Energy Sciences under contract no. DE-AC02-06CH11357. MRCAT operations, beamlines 10-BM and 10-ID, are supported by the Department of Energy and the MRCAT member institutions.

REFERENCES

(1) Lavrenov, A. V.; Saifulina, L. F.; Buluchevskii, E. A.; Bogdanets, E. N. Propylene production technology: Today and tomorrow. *Catal. Ind.* **2015**, *7*, 175−187.

(2) Ren, T.; Patel, M.; Blok, K. Olefins from conventional and heavy feedstocks: Energy use in steam cracking and alternative processes. *Energy* **2006**, *31*, 425−451.

(3) Sattler, J. J. H. B.; Ruiz-Martinez, J.; Santillan-Jimenez, E.; Weckhuysen, B. M. Catalytic Dehydrogenation of Light Alkanes on Metal and Metal oxides. *Chem. Rev.* **2014**, *114*, 10613−10653.

(4) Benco, L.; Bucko, T.; Hafner, J. Dehydrogenation of propane over Zn-MOR. Static and dynamic reaction energy diagram. *J. Catal.* **2011**, *277*, 104−116.

(5) Dixit, M.; Kostetskyy, P.; Mpourmpakis, G. Structure-Activity Relationships in Alkane Dehydrogenation on γ-Al_2O_3: Site-Dependent Reactions. *ACS Catal.* **2018**, *8*, 11570−11578.

(6) Li, Q.; Sui, Z. J.; Zhou, X. G.; Chen, D. Kinetics of Propane Dehydrogenation over Pt-Sn/Al_2O_3 Catalyst. *Appl. Catal., A* **2011**, *398*, 18−26.

(7) Kaylor, N.; Davis, R. J. Propane dehydrogenation over supported Pt-Sn nanoparticles. *J. Catal.* **2018**, *367*, 181−193.

(8) Sattler, J. J. H. B.; González-Jiménez, I. D.; Mens, A. M.; Arias, M.; Visser, T.; Weckhuysen, B. M. Operando UV-Vis spectroscopy of a catalytic solid in a pilot-scale reactor: deactivation of a CrO_x/Al_2O_3 propane dehydrogenation catalyst. *Chem. Commun.* **2013**, *49*, 1518−1520.

(9) Zhang, Z. W.; He, D. D.; Huang, Z. J.; He, S. F.; Lu, J. C.; Luo, Y. M. Flowing-Air-Induced Transformation to Promote the Dispersion of the CrO_x Catalyst for Propane Dehydrogenation. *ACS Appl. Mater. Interfaces* **2021**, *13*, 19873−19883.

(10) Seemakurthi, R. R.; Canning, G.; Wu, Z. W.; Miller, J. T.; Datye, A. K.; Greeley, J. Identification of a Selectivity Descriptor for Propane Dehydrogenation through Density Functional and Microkinetic Analysis on Pure Pd and Pd Alloys. *ACS Catal.* **2021**, *11*, 9588−9604.

(11) Zhang, W.; Wang, H. Z.; Jiang, J. W.; Sui, Z. J.; Zhu, Y. A.; Chen, D.; Zhou, X. G. Size Dependence of Pt Catalysts for Propane Dehydrogenation: from Atomically Dispersed to Nanoparticles. *ACS Catal.* **2020**, *10*, 12932−12942.

(12) Zhu, J.; Yang, M. L.; Yu, Y. D.; Zhu, Y. A.; Sui, Z. J.; Zhou, X. G.; Holmen, A.; Chen, D. Size-Dependent Reaction Mechanism and Kinetics for Propane Dehydrogenation over Pt Catalysts. *ACS Catal.* **2015**, *5*, 6310−6319.

(13) Deng, L. D.; Miura, H.; Shishido, T.; Hosokawa, S.; Teramura, K.; Tanaka, T. Strong metal-support interaction between Pt and SiO_2 following high-temperature reduction: a catalytic interface for propane dehydrogenation. *Chem. Commun.* **2017**, *53*, 6937−6940.

(14) Chen, X. W.; Peng, M.; Cai, X. B.; Chen, Y. L.; Jia, Z. M.; Deng, Y. C.; Mei, B. B.; Jiang, Z.; Xiao, D. Q.; Wen, X. D.; Wang, N.; Liu, H. Y.; Ma, D. Regulating coordination number in atomically dispersed Pt species on defect-rich graphene for n-butane dehydrogenation reaction. *Nat. Commun.* **2021**, *12*, 2664.

(15) Zhang, J. Y.; Deng, Y. C.; Cai, X. B.; Chen, Y. L.; Peng, M.; Jia, Z. M.; Jiang, Z.; Ren, P. J.; Yao, S. Y.; Xie, J. L.; Xiao, D. Q.; Wen, X. D.; Wang, N.; Liu, H. Y.; Ma, D. Tin-Assisted Fully Exposed Platinum Clusters Stabilized on Defect-Rich Graphene for Dehydrogenation Reaction. *ACS Catal.* **2019**, *9*, 5998−6005.

(16) Motagamwala, A. H.; Almallahi, R.; Wortman, J.; Igenegbai, V. O.; Linic, S. Stable and selective catalysts for propane dehydrogenation operating at thermodynamic limit. *Science* **2021**, *373*, 217−222.

(17) Ma, S. C.; Liu, Z. P. Zeolite-confined subnanometric PtSn mimicking mortise-and-tenonjoinery for catalytic propane dehydrogenation. *Nat. Commun.* **2022**, *13*, 2716.

(18) Chen, S.; Zhao, Z. J.; Mu, R. T.; Chang, X.; Luo, J.; Purdy, S. C.; Kropf, A. J.; Sun, G. D.; Pei, C. L.; Miller, J. T.; Zhou, X. H.; Vovk, E.; Yang, Y.; Gong, J. L. Propane Dehydrogenation on Single-Site [$PtZn_4$] Intermetallic Catalysts. *Chem* **2021**, *7*, 387−405.

(19) Sun, Q. M.; Wang, N.; Fan, Q. Y.; Zeng, L.; Mayoral, A.; Miao, S.; Yang, R. O.; Jiang, Z.; Zhou, W.; Zhang, J. C.; Zhang, T. J.; Xu, J.; Zhang, P.; Cheng, J.; Yang, D. C.; Jia, R.; Li, L.; Zhang, Q. H.; Wang, Y.; Terasaki, O.; Yu, J. H. Subnanometer Bimetallic Platinum-Zinc clusters in Zeolites for Propane Dehydrogenation. *Angew. Chem., Int. Ed.* **2020**, *132*, 19618−19627.

(20) Ryoo, R.; Kim, J.; Jo, C.; Han, S. W.; Kim, J. C.; Park, H.; Han, J.; Shin, H. S.; Shin, J. W. Rare-earth-platinum alloy nanoparticles in mesoporous zeolite for catalysis. *Nature* **2020**, *585*, 221−224.

(21) Nakaya, Y.; Xing, F. L.; Ham, H.; Shimizu, K.; Furukawa, S. Doubly Decorated Platinum-Gallium Intermetallics as Stable Catalysts for Propane Dehydrogenation. *Angew. Chem., Int. Ed.* **2021**, *133*, 19867−19871.

(22) Payard, P. A.; Rochlitz, L.; Searles, K.; Foppa, L.; Leuthold, B.; Safonova, O. V.; Comas-Vives, A.; Copéret, C. Dynamics and Site Isolation: Keys to High Propane Dehydrogenation Performance of Silica-Supported PtGa Nanoparticles. *JACS Au* **2021**, *1*, 1445−1458.

(23) Sun, G. D.; Zhao, Z. J.; Mu, R. T.; Zha, S. J.; Li, L. L.; Chen, S.; Zhang, K. T.; Luo, J.; Li, Z. L.; Purdy, S. C.; Kropf, A. J.; Miller, J. T.; Zeng, L.; Gong, J. L. Breaking the scaling relationship via thermally stable Pt/Cu single atom alloy for catalytic dehydrogenation. *Nat. Commun.* **2018**, *9*, 4454.

(24) Escorcia, N. J.; Libretto, N. J.; Miller, J. T.; Li, C. W. Colloidal Synthesis of Well-Defined Bimetallic Nanoparticles for Nonoxidative Alkane Dehydrogenation. *ACS Catal.* **2020**, *10*, 9813−9823.

(25) Wu, Z. W.; Bukowski, B. C.; Li, Z.; Milligan, C.; Zhou, L.; Ma, T.; Wu, Y.; Ren, Y.; Ribeiro, F. H.; Delgass, W. N.; Greeley, J.; Zhang, G. H.; Miller, J. T. Changes in Catalytic and Adsorptive Properties of 2 nm Pt_3Mn Nanoparticles by Subsurface Atoms. *J. Am. Chem. Soc.* **2018**, *140*, 14870−14877.

(26) Dai, Y. H.; Gu, J. J.; Tian, S. Y.; Wu, Y.; Chen, J. C.; Li, F. X.; Du, Y. H.; Peng, L. M.; Ding, W. P.; Yang, Y. H. γ-Al_2O_3 sheet-stabilized isolate Co^{2+} for catalytic propane dehydrogenation. *J. Catal.* **2020**, *381*, 482−492.

(27) Wu, L. Z.; Ren, Z. Z.; He, Y. S.; Yang, M.; Yu, Y. K.; Liu, Y. M.; Tan, L.; Tang, Y. Atomically Dispersed Co^{2+} Sites Incorporated into a Silicalite-1 Zeolite Framework as a High-Performance and Coking-Resistant Catalyst for Propane Nonoxidative Dehydrogenation to Propylene. *ACS Appl. Mater. Interfaces* **2021**, *13*, 48934−48948.

(28) Nozik, D.; Tinga, F. M. P.; Bell, A. T. Propane Dehydrogenation and Cracking over Zn/H-MFI Prepared by Solid-State Ion Exchange of $ZnCl_2$. *ACS Catal.* **2021**, *11*, 14489−14506.

(29) Schweitzer, N. M.; Hu, B.; Das, U.; Kim, H.; Greeley, J.; Curtiss, L. A.; Stair, P. C.; Miller, J. T.; Hock, A. S. Propylene Hydrogenation and Propane Dehydrogenation by a Single-Site Zn^{2+} on Silica Catalyst. *ACS Catal.* **2014**, *4*, 1091−1098.

(30) Sharma, L.; Jiang, X.; Wu, Z. L.; DeLaRiva, A.; Datye, A. K.; Baltrus, J.; Rangarajan, S.; Baltrusaitis, J. Atomically Dispersed Tin-Modified γ-alumina for Selective Propane Dehydrogenation under H_2S Co-feed. *ACS Catal.* **2021**, *11*, 13472−13482.

(31) Yue, Y. Y.; Fu, J.; Wang, C. M.; Yuan, P.; Bao, X. J.; Xie, Z. L.; Basset, J. M.; Zhu, H. B. Propane dehydrogenation catalyzed by single Lewis acid site in Sn-Beta zeolite. *J. Catal.* **2021**, *395*, 155−167.

(32) Searles, K.; Siddiqi, G.; Safonova, O. V.; Copéret, C. Silica-supported isolated gallium sites as highly active, selective and stable propane dehydrogenation catalysts. *Chem. Sci.* **2017**, *8*, 2661−2666.

(33) Robbins, J. P.; Ezeonu, L.; Tang, Z. Y.; Yang, X. F.; Koel, B. E.; Podkolzin, S. G. Propane Dehydrogenation to Propylene and Propylene Adsorption on Ni and Ni-Sn Catalysts. *ChemCatChem* **2022**, *14*, No. e202101546.

(34) Yan, Z.; Goodman, D. W. Silica-Supported Au-Ni Catalysts for the Dehydrogenation of Propane. *Catal. Lett.* **2012**, *142*, 517−520.

(35) Xu, Y. L.; Sang, H. X.; Wang, K.; Wang, X. T. Catalytic dehydrogenation of isobutene in the presence of hydrogen over Cs-modified Ni_2P supported on active carbon. *Appl. Surf. Sci.* **2014**, *316*, 163−170.

(36) Zhu, Q. Q.; Zhang, H. L.; Zhang, S.; Wang, G. W.; Zhu, X. L.; Li, C. Y. Dehydrogenation of Isobutene over a Ni-P/SiO_2 Catalyst: Effect of P Addition. *Ind. Eng. Chem. Res.* **2019**, *58*, 7834−7843.

(37) Resasco, D. E.; Marcus, B. K.; Huang, C. S.; Durante, V. A. Isobutane dehydrogenation over sulfided nickel catalysts. *J. Catal.* **1994**, *146*, 40−55.

(38) Wang, G. W.; Meng, Z.; Liu, J. W.; Li, C. Y.; Shan, H. H. Promoting Effect of Sulfur Addition on the Catalytic Performance of $Ni/MgAl_2O_4$ Catalysts for Isobutane Dehydrogenation. *ACS Catal.* **2013**, *3*, 2992−3001.

(39) Metzger, E. D.; Comito, R. J.; Hendon, C. H.; Dincă, M. Mechanism of Single-Site Molecule-Like Catalytic Ethylene Dimerization in Ni-MFU-4l. *J. Am. Chem. Soc.* **2017**, *139*, 757−762.

(40) Li, Y.; Adli, N. M.; Shan, W. T.; Wang, M. Y.; Zachman, M. J.; Hwang, S.; Tabassum, H.; Karakalos, S.; Feng, Z. X.; Wang, G. F.; Li, Y. G. C.; Wu, G. Atomically dispersed single Ni site catalysts for high-efficiency CO_2 electroreduction at industrial-level current densities. *Energy Environ. Sci.* **2022**, *15*, 2108−2119.

(41) Pattengale, B.; Huang, Y. C.; Yan, X. X.; Yang, S. Z.; Younan, S.; Hu, W. H.; Li, Z. D.; Lee, S.; Pan, X. Q.; Gu, J.; Huang, J. E. Dynamic evolution and reversibility of single-atom Ni(II) active site in 1T-MoS_2 electrocatalysts for hydrogen evolution. *Nat. Commun.* **2020**, *11*, 4114.

(42) Streitz, F. H.; Mintmire, J. W. Energetics of aluminum vacancies in gamma alumina. *Phys. Rev. B* **1999**, *60*, 773.

(43) Maglia, F.; Gennari, S.; Buscaglia, V. Energetics of Aluminum Vacancies and Incorporation of Foreign Trivalent Ions in γ-Al_2O_3: An Atomistic Simulation Study. *J. Am. Ceram. Soc.* **2008**, *91*, 283−290.

(44) Prins, R. On the structure of γ-Al_2O_3. *J. Catal.* **2020**, *392*, 336−346.

(45) Wang, J. A.; Morales, A.; Bokhimi, X.; Novaro, O.; López, T.; Gómez, R. Cationic and Anionic Vacancies in the Crystalline Phases of Sol-Gel Magnesia-Alumina Catalysts. *Chem. Mater.* **1999**, *11*, 308−313.

(46) Wang, J. A.; Bokhimi, X.; Morales, A.; Novaro, O.; López, T.; Gómez, R. Aluminum Local Environment and Defects in the Crystalline Structure of Sol-Gel Alumina Catalyst. *J. Phys. Chem. B* **1999**, *103*, 299−303.

(47) Peterson, E. J.; DeLaRiVa, A. T.; Li, S.; Johnson, R. S.; Guo, H.; Miller, J. T.; Kwak, J. H.; Peden, C. H. F.; Kiefer, B.; Allard, L. F.; Ribeiro, F. H.; Datye, A. K. Low-temperature carbon monoxide oxidation catalysed by regenerable atomically dispersed palladium on alumina. *Nat. Commun.* **2014**, *5*, 4885.

(48) Rogers, J. L.; Mangarella, M. C.; D'Amico, A. D.; Gallagher, J. R.; Dutzer, M. R.; Stavitski, E.; Miller, J. T.; Sievers, C. Differences in the Nature of Active Sites for Methane Dry Reforming and Methane Steam Reforming over Nickel Aluminate Catalysts. *ACS Catal.* **2016**, *6*, 5873−5886.

(49) Ressler, T. *WinXAS*: A Program for X-ray Absorption Spectroscopy Data Analysis under MS-Windows. *J. Synchrotron Radiat.* **1998**, *5*, 118−122.

(50) Lear, T.; Marshall, R.; Lopez-Sanchez, J. A.; Jackson, S. D. The application of infrared spectroscopy to probe the surface morphology of alumina-supported palladium catalysts. *J. Chem. Phys.* **2005**, *123*, 174706.

(51) Im, J.; Choi, M. Physicochemical Stabilization of Pt Against Sintering for a Dehydrogenation Catalyst with High Activity, Selectivity, and Durability. *ACS Catal.* **2016**, *6*, 2819−2826.

(52) Pakharukova, V. P.; Yatsenko, D. A.; Gerasimov, E. Y.; Shalygin, A. S.; Martyanov, O. N.; Tsybulya, S. V. Coherent 3D nanostructure of γ-Al_2O_3: Simulation of whole X-ray powder diffraction pattern. *J. Solid State Chem.* **2017**, *246*, 284−292.

(53) Ragupathi, C.; Vijaya, J. J.; Surendhar, P.; Kennedy, L. J. Comparative investigation of nickel aluminate ($NiAl_2O_4$) nano and microstructures for the structural, optical and catalytic properties. *Polyhedron* **2014**, *72*, 1−7.

(54) Lu, J. C.; Lei, Y. Q.; Wan, G. P.; Mei, Z. Q.; Yu, J.; Zhao, Y.; He, S. F.; Luo, Y. M. Weakening the metal-support strong interaction to enhance catalytic performances of alumina supported Ni-based catalysts for producing hydrogen. *Appl. Catal., B* **2020**, *263*, No. 118177.

(55) Yang, R. C.; Li, X. G.; Wu, J. S.; Zhang, X.; Zhang, Z. H.; Cheng, Y. F.; Guo, J. T. Hydrotreating of crude 2-ethylhexanol over Ni/Al_2O_3 catalysts: Surface Ni species-catalytic activity correlation. *Appl. Catal., A* **2009**, *368*, 105−112.

(56) Xiang, L.; Gong, Y. L.; Li, J. C.; Wang, Z. W. Influence of hydrothermal modification on the properties of Ni/Al_2O_3 catalyst. *Appl. Surf. Sci.* **2004**, *239*, 94−100.

(57) Yang, H. B.; Hung, S. F.; Liu, S.; Yuan, K. D.; Miao, S.; Zhang, L. P.; Huang, X.; Wang, H. Y.; Cai, W. Z.; Chen, R.; Gao, J. J.; Yang, X. F.; Chen, W.; Huang, Y. Q.; Chen, H. M.; Li, C. M.; Zhang, T.; Liu, B. Atomically dispersed Ni(I) as the active site for electrochemical CO_2 reduction. *Nat. Energy* **2018**, *3*, 140−147.

(58) Zhang, G.; Yang, C.; Miller, J. T. Tetrahedral Nickel(II) phosphosilicate single-site selective propane dehydrogenation catalyst. *ChemCatChem* **2018**, *10*, 961−964.

(59) Groppo, E.; Prestipino, C.; Cesano, F.; Bonino, F.; Bordiga, S.; Lamberti, C.; Thüne, P. C.; Niemantsverdriet, J. W.; Zecchina, A. In situ, Cr *K*-edge XAS study on the Phillips catalyst: activation and ethylene polymerization. *J. Catal.* **2005**, *230*, 98−108.

(60) Gruver, V.; Fripiat, J. J. Lewis Acid Sites and Surface Aluminum in Aluminas and Mordenites: An Infrared Study of CO Chemisorption. *J. Phys. Chem.* **1994**, *98*, 8549−8554.

(61) Layman, K. A.; Bussell, M. E. Infrared Spectroscopic Investigation of CO Adsorption on Silica-Supported Nickel Phosphide Catalysts. *J. Phys. Chem. B* **2004**, *108*, 10930−10941.

(62) Zacharaki, E.; Beato, P.; Tiruvalam, R. R.; Andersson, K. J.; Fjellvåg, H.; Sjåstad, A. O. From Colloidal Monodisperse Nickel Nanoparticles to Well-Defined Ni/Al_2O_3 Model Catalysts. *Langmuir* **2017**, *33*, 9836−9843.

(63) Resini, C.; Venkov, T.; Hadjiivanov, K.; Presto, S.; Riani, P.; Marazza, R.; Ramis, G.; Busca, G. An FTIR study of the dispersed Ni species on Ni-YSZ catalysts. *Appl. Catal., A* **2009**, *353*, 137−143.

(64) Ma, C.; Du, Y. Y.; Feng, J. T.; Cao, X. Z.; Yang, J.; Li, D. Q. Fabrication of supported PdAu nanoflower catalyst for partial hydrogenation of acetylene. *J. Catal.* **2014**, *317*, 263−271.

(65) Peri, J. B. Infrared studies of Ni held at low concentrations on alumina supports. *J. Catal.* **1984**, *86*, 84−94.

(66) Basu, P.; Panayotov, D.; Yates, J. T. Rhodium-carbon monoxide surface chemistry: the involvement of surface hydroxyl groups on alumina and silica supports. *J. Am. Chem. Soc.* **1988**, *110*, 2074−2081.

(67) Nishimura, M.; Thomas, J. M. IR study of the interaction of hydroxyl groups of silica gel with Cr species of Phillips' type catalysts. *Catal. Lett.* **1993**, *21*, 149−155.

(68) Fricke, C.; Rajbanshi, B.; Walker, E. A.; Terejanu, G.; Heyden, A. Propane Dehydrogenation on Platinum Catalysts: Identifying the Active Sites through Bayesian Analysis. *ACS Catal.* **2022**, *12*, 2487−2498.

(69) Otroshchenko, T.; Sokolov, S.; Stoyanova, M.; Kondratenko, V. A.; Rodemerck, U.; Linke, D.; Doz, P.; Kondratenko, E. V. ZrO_2-Based Alternatives to Conventional Propane Dehydrogenation Catalysts: Active Sites, Design, and Performance. *Angew. Chem., Int. Ed.* **2015**, *54*, 15880−15883.

(70) Lian, Z.; Si, C. W.; Jan, F.; Zhi, S. K.; Li, B. Coke Deposition on Pt-Based Catalysts in Propane Direct Dehydrogenation: Kinetics, Suppression, and Elimination. *ACS Catal.* **2021**, *11*, 9279−9292.

(71) Wang, H. Z.; Sun, L. L.; Sui, Z. J.; Zhu, Y. A.; Ye, G. H.; Chen, D.; Zhou, X. G.; Yuan, W. K. Coke Formation on Pt-Sn/Al_2O_3 Catalyst for Propane Dehydrogenation. *Ind. Eng. Chem. Res.* **2018**, *57*, 8647−8654.